

# MAP AS A PROMPT: LEARNING MULTI-MODAL SPATIAL-SIGNAL FOUNDATION MODELS FOR CROSS-SCENARIO WIRELESS LOCALIZATION

006 **Anonymous authors**

007 Paper under double-blind review

## ABSTRACT

013 Accurate and robust wireless localization is a critical enabler for emerging 5G/6G  
 014 applications, including autonomous driving, extended reality, and smart manu-  
 015 facturing. Despite its importance, achieving precise localization across diverse  
 016 environments remains challenging due to the complex nature of wireless signals  
 017 and their sensitivity to environmental changes. Existing data-driven approaches  
 018 often suffer from limited generalization capability, requiring extensive labeled  
 019 data and struggling to adapt to new scenarios. To address these limitations, we  
 020 propose SigMap, a multimodal foundation model that introduces two key innova-  
 021 tions: (1) A cycle-adaptive masking strategy that dynamically adjusts masking  
 022 patterns based on channel periodicity characteristics to learn robust wireless repre-  
 023 sentations; (2) A novel "map-as-prompt" framework that integrates 3D geographic  
 024 information through lightweight soft prompts for effective cross-scenario adapta-  
 025 tion. Extensive experiments demonstrate that our model achieves state-of-the-art  
 026 performance across multiple localization tasks while exhibiting strong zero-shot  
 027 generalization in unseen environments, significantly outperforming both super-  
 028 vised and self-supervised baselines by considerable margins.

## 1 INTRODUCTION

031 Wireless localization has evolved from classical model-based methods to data-driven deep learning  
 032 approaches, and more recently, to paradigms built upon foundation models and large language mod-  
 033 els (LLMs). Despite these advances, existing techniques continue to face significant challenges in  
 034 complex environments—particularly under non-line-of-sight (NLoS) conditions and in rich multi-  
 035 path scenarios—due to limitations in representation learning and environmental reasoning.

036 Traditional localization systems rely on geometric or signal-strength measurements such as time-  
 037 of-arrival (ToA), time-difference-of-arrival (TDoA), angle-of-arrival (AoA), and received signal  
 038 strength (RSS) (Chen et al., 2022a). Classical algorithms including MUSIC and OMP are widely  
 039 adopted for parameter estimation (Keskin et al., 2021). However, such model-based methods assume  
 040 idealized propagation conditions and perform poorly in urban settings with substantial multipath and  
 041 NLoS effects, often incurring errors over 100 meters (Chen et al., 2024). Although some works at-  
 042 tempt to mitigate NLoS via filtering or hardware enhancements (Huang et al., 2023; Zhou et al.,  
 043 2019), they typically overlook richer environmental semantics from maps or channel characteristics.

044 To address these issues, data-driven methods have been extensively explored. Supervised models  
 045 such as MLPs (Gao et al., 2023), CNNs (Wu et al., 2021), and LSTMs (Chen et al., 2023) learn  
 046 direct mappings from channel state information (CSI) to user positions. While effective in specific  
 047 settings, they require large labeled datasets and exhibit limited cross-environment generalization  
 048 (Pan et al., 2025). Subsequent semi-supervised and unsupervised approaches—using autoencoders,  
 049 GANs, and domain adaptation (Ruan et al., 2023; Chen et al., 2022b; Junoh & Pyun, 2024; Li et al.,  
 050 2021)—aim to reduce labeling costs, yet often fail to learn robust and transferable representations  
 051 that capture high-level semantic features of the environment.

052 Recent efforts have turned toward self-supervised learning (SSL) and foundation models inspired  
 053 by successes in NLP and vision. Methods such as LWM (Alikhani et al., 2024) and WirelessGPT  
 (Yang et al., 2025) employ masked channel modeling to learn general-purpose channel representa-

054 tions, while contrastive learning frameworks (Salihu et al., 2024) extract invariant channel features.  
 055 However, these models are not designed specifically for localization and often lack task-aware semantic  
 056 understanding. Several SSL-based frameworks target localization more directly, including  
 057 CrowdBERT (Han et al., 2024) and signal-guided masked autoencoders (Wang et al., 2025), which  
 058 adopt masking strategies for reconstructing RSS or channel impulse responses (CIR). Despite their  
 059 potential, such approaches are often confined to specific configurations and rely on single SSL ob-  
 060 jectives, limiting the diversity and generalizability of the learned features.

061 Concurrently, LLMs have been introduced to the wireless domain. For example, WirelessLLM  
 062 (Shao et al., 2024) incorporates domain knowledge via prompt engineering and retrieval-augmented  
 063 generation. Although effective for high-level protocol reasoning, LLMs struggle with low-level sig-  
 064 nal processing and often produce hallucinations when applied to channel-based inference, restricting  
 065 their applicability to precise localization tasks.

### 067 1.1 RESEARCH GAPS

069 Current wireless localization methods face two fundamental limitations:

- 071 • **Inadequate Handling of Signal Periodicity:** Existing self-supervised approaches employ  
 072 generic masking strategies that ignore the inherent cyclic patterns in Channel State Infor-  
 073 mation (CSI). This allows models to exploit local periodic shortcuts rather than learning  
 074 meaningful global representations of signal propagation.
- 075 • **Superficial Geographic Integration:** While some methods incorporate basic map data,  
 076 they fail to capture the rich spatial-topological relationships in 3D environments. The fu-  
 077 sion between geometric constraints and channel representations remains shallow and lacks  
 078 interpretability.

### 080 1.2 CONTRIBUTIONS

082 This work addresses these gaps through three key contributions:

- 084 • **Cycle-Adaptive Masked Modeling:** We introduce a novel masking strategy that dyna-  
 085 mically adapts to CSI periodicity by computing row-wise cross-correlation and generating  
 086 shift-aware patterns. This disrupts periodic shortcuts and forces learning of globally mean-  
 087 ingful signal representations.
- 088 • **Map-Conditioned Prompt Tuning:** We develop a geographic prompt mechanism that en-  
 089 codes 3D map information via graph neural networks. These prompts enable interpretable  
 090 fusion of environmental constraints during fine-tuning, enhancing accuracy in complex  
 091 multipath scenarios.
- 092 • **Parameter-Efficient Generalization:** Our foundation model achieves state-of-the-art per-  
 093 formance with limited labeled data and demonstrates strong zero-shot generalization to  
 094 unseen environments and base station configurations.

## 096 2 PRELIMINARIES

099 This section introduces the core concepts of wireless channel modeling and formally defines the lo-  
 100 calization problem. The physical principles explained here are directly leveraged by our geographic  
 101 prompt tuning method.

### 103 2.1 WIRELESS CHANNEL MODELING FOR LOCALIZATION

105 The fundamental premise of our work is that Channel State Information (CSI) contains geometric  
 106 relationships between transmitters and receivers. As shown in Figure 1, wireless signals propagate  
 107 through Line-of-Sight (LoS) and Non-Line-of-Sight (NLoS) paths, creating unique spatial finger-  
 prints in the CSI data.

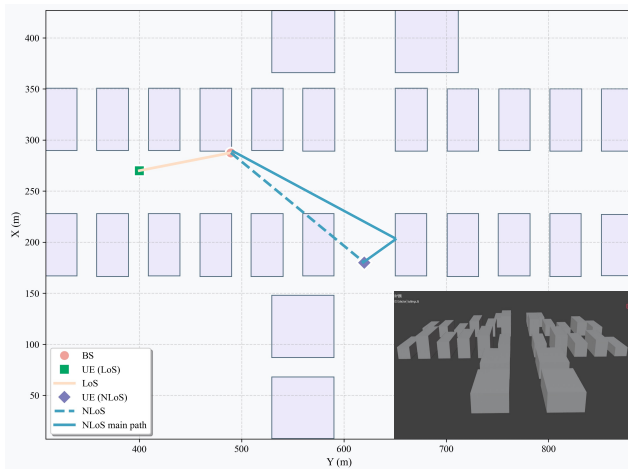


Figure 1: Wireless propagation paths in urban environments. LoS represents direct propagation, while NLoS paths result from reflections and diffractions. **Bottom-right inset:** corresponding 3D map visualization showing the same LoS/NLoS topology used for prompt generation.

For a MIMO-OFDM system with  $N_t$  transmit antennas and  $N_r$  receive antennas, the CSI matrix  $\mathbf{H}[k] \in \mathbb{C}^{N_r \times N_t}$  at subcarrier  $k$  can be expressed as the superposition of both LoS and NLoS components:

$$\mathbf{H}[k] = \underbrace{\alpha_{\text{LoS}} e^{-j2\pi\tau_{\text{LoS}}f_k} \mathbf{a}_r(\theta_{\text{LoS}}^r) \mathbf{a}_t(\theta_{\text{LoS}}^t)^H}_{\text{LoS component}} + \underbrace{\sum_{l=1}^{L_{\text{NLoS}}} \alpha_l e^{-j2\pi\tau_l f_k} \mathbf{a}_r(\theta_l^r) \mathbf{a}_t(\theta_l^t)^H}_{\text{NLoS components}} \quad (1)$$

where  $L_{\text{NLoS}}$  denotes the number of NLoS multipath components,  $\alpha_l$  and  $\tau_l$  represent the complex gain and delay of the  $l$ -th path,  $f_k$  is the frequency of the  $k$ -th subcarrier, and  $\mathbf{a}_r(\theta_l^r)$ ,  $\mathbf{a}_t(\theta_l^t)$  are the array steering vectors at receiver and transmitter, respectively.

The key insight for localization is that each path in equation 1 carries geometric information. Single-base station localization is possible because CSI contains time delay (related to distance) and angle information that can define a spatial vector. Multipath effects provide multiple such constraints, enabling rough positioning even without precise time measurements. Multi-base station setups provide richer information by offering diverse spatial perspectives.

## 2.2 RAY-TRACING AND MAP ALIGNMENT

We use ray-tracing to generate realistic training data that captures the mapping between physical geometry and wireless channels. The process can be abstracted as:

$$(\mathbf{p}_{\text{BS}}, \mathbf{p}_{\text{UE}}, \mathcal{M}) \xrightarrow{\text{Ray-tracing}} \mathbf{H}_{\text{CSI}} \quad (2)$$

where  $\mathbf{p}_{\text{BS}}$  is the base station position,  $\mathbf{p}_{\text{UE}}$  is the user position, and  $\mathcal{M}$  is the 3D environment map.

The map  $\mathcal{M}$  serves two crucial purposes: 1) generating physically realistic training data, and 2) providing geometric constraints during inference to resolve multipath ambiguity. This alignment process helps decompose raw CSI into its constituent LoS and NLoS components, which is learned implicitly by our model through geographic prompt tuning.

## 2.3 PROBLEM FORMULATION: WIRELESS LOCALIZATION

We define the wireless localization problem as estimating user equipment position from channel measurements and environmental context.

**Inputs:**

162 • Channel State Information  $\mathbf{H} \in \mathbb{C}^{N_r \times N_t \times N_{sc}}$  from one or multiple base stations  
 163 • 3D environment map  $\mathcal{M}$  containing building geometries  
 164 • Base station positions  $\mathbf{P}_{\text{BS}} = \{\mathbf{p}_{\text{BS}}^{(1)}, \dots, \mathbf{p}_{\text{BS}}^{(T)}\}$

165  
 166  
**167 Output:** Estimated user position  $\hat{\mathbf{p}}_{\text{UE}} \in \mathbb{R}^3$ .  
 168  
**169 Objective:** Learn a mapping function  $f_{\theta}$  that minimizes:

170 
$$\mathbb{E} [\|f_{\theta}(\mathbf{H}, \mathcal{M}, \mathbf{P}_{\text{BS}}) - \mathbf{p}_{\text{UE}}\|^2] \quad (3)$$
  
 171

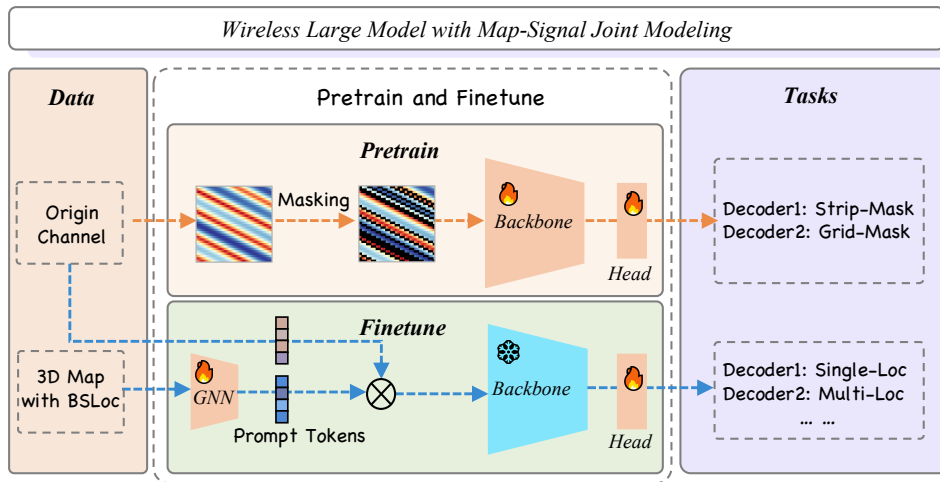
172 The inclusion of map information  $\mathcal{M}$  differentiates our approach from conventional CSI-only meth-  
 173 ods, enabling more accurate and physically consistent localization.  
 174

### 175 3 METHODOLOGY

#### 177 3.1 OVERALL FRAMEWORK

179 Our proposed wireless localization foundation model addresses the fundamental challenge of achiev-  
 180 ing accurate positioning across diverse environments with minimal labeled data requirements. The  
 181 framework follows a two-stage learning paradigm consisting of self-supervised pre-training on un-  
 182 labeled CSI data followed by prompt-based fine-tuning for specific localization tasks. This approach  
 183 enables the model to learn general-purpose representations of wireless signal propagation that can  
 184 be efficiently adapted to new environments.

185 As illustrated in Figure 2, the framework integrates three core components: (1) a transformer-based  
 186 backbone network that captures long-range dependencies in CSI data, (2) a novel cycle-adaptive  
 187 masked modeling strategy that prevents shortcut learning in periodic signals, and (3) a geographic  
 188 prompt tuning mechanism that incorporates environmental constraints during fine-tuning. The key  
 189 innovation lies in our cycle-aware masking approach that dynamically adapts to signal periodicity,  
 190 combined with map-conditioned prompts that enable efficient adaptation with minimal parameter  
 191 updates.



208 Figure 2: Overall architecture of our wireless localization foundation model, showing the two-stage  
 209 learning process with self-supervised pre-training and prompt-based fine-tuning.  
 210

#### 212 3.2 SIGNAL REPRESENTATION AND PREPROCESSING

214 Wireless Channel State Information (CSI) provides a rich characterization of the propagation environ-  
 215 ment by capturing multipath effects, fading characteristics, and spatial diversity. In multi-antenna  
 OFDM systems, we represent the channel frequency response as a complex-valued tensor:

216  
217  
218

$$\mathcal{H} \in \mathbb{C}^{N_r \times N_t \times N_s} \quad (4)$$

219 where  $N_r$ ,  $N_t$ , and  $N_s$  denote the number of receive antennas, transmit antennas, and subcarriers  
220 respectively. Each element  $h_{i,j}[k]$  represents the complex channel gain between specific antenna  
221 pairs at different subcarriers.

222 To facilitate deep learning processing while preserving critical phase information, we transform the  
223 complex CSI data into a real-valued representation through channel-wise separation:  
224

$$\mathbf{X} = [\Re(\mathcal{H}), \Im(\mathcal{H})] \in \mathbb{R}^{2 \times N_r \times N_t \times N_s} \quad (5)$$

225 This representation maintains the spatial and frequency diversity essential for accurate localization  
226 while being compatible with standard neural network operations.  
227

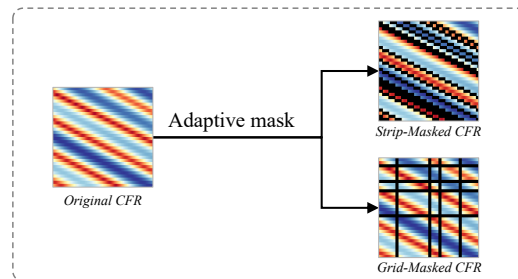
### 230 3.3 CYCLE-ADAPTIVE MASKED MODELING 231

232 Traditional masked autoencoding approaches often struggle with wireless signals due to their in-  
233 herent periodic patterns, which can be exploited as learning shortcuts. Our cycle-adaptive mask-  
234 ing strategy addresses this limitation by dynamically generating mask patterns that disrupt periodic  
235 structures while preserving semantically meaningful information.

236 The core insight is to detect dominant periodicities in the CSI data and generate masks that prevent  
237 simple interpolation-based reconstruction. For each input sample, we compute shift patterns using  
238 cross-correlation analysis and generate adaptive mask patterns:  
239

$$240 \quad \mathbf{M}_{\text{cycle}}[i, j] = \begin{cases} 0 & \text{if } |j - (j_0 + i \cdot d_{\text{final}})| \leq w \\ 1 & \text{otherwise} \end{cases} \quad (6)$$

241 where  $d_{\text{final}}$  represents the detected periodicity shift,  $j_0$  is the starting offset, and  $w$  controls the  
242 mask width. This approach ensures that the model must learn meaningful signal representations  
243 rather than relying on pattern repetition, as illustrated in Figure 3.  
244



245 Figure 3: Illustration of our cycle-adaptive masking strategy. The mask pattern (right) is dynamically  
246 generated based on the detected periodicity in the CSI amplitude data (left), preventing the model  
247 from exploiting simplistic periodic shortcuts.

248 The reconstruction objective trains the model to recover the original signal from masked inputs:  
249

$$250 \quad \mathcal{L}_{\text{MAE}} = \mathbb{E}_{\mathbf{X}} [\|\mathbf{X} - f_{\theta_{\text{dec}}}(\mathbf{X}_{\text{masked}})\|^2] \quad (7)$$

### 251 3.4 GEOGRAPHIC PROMPT TUNING 252

253 Following pre-training, we employ a parameter-efficient fine-tuning strategy that leverages geo-  
254 graphic information from 3D environment models. The core innovation is the transformation of  
255 spatial relationships between buildings and base stations into a set of learnable prompt tokens that  
256 guide the pre-trained model without updating its core parameters.

270 **Algorithm 1** Geographic Prompt Generation

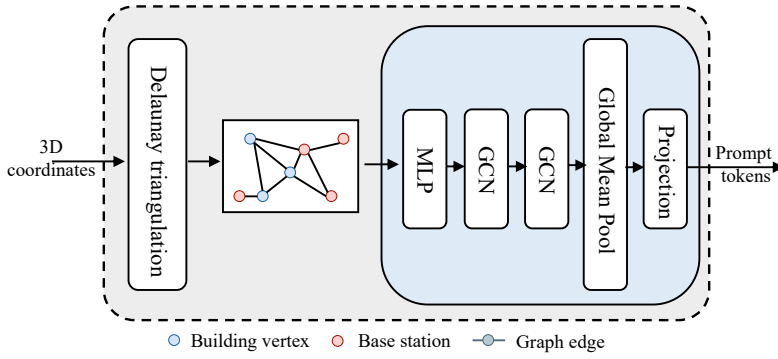
---

```

271 1: procedure GENERATEGEO_PROMPT( $\mathcal{M}$ ,  $\mathbf{P}_{\text{BS}}$ )
272 2:    $\mathbf{h}_v^{(0)} = \text{MLP}_{\text{vert}}(\mathbf{v}; \mathbf{W}_{\text{vert}})$  ▷ Encode vertex positions
273 3:    $\mathbf{h}_{\text{BS}}^{(0)} = \text{MLP}_{\text{BS}}(\mathbf{p}_{\text{BS}}; \mathbf{W}_{\text{bs}})$  ▷ Encode BS positions
274 4:    $\mathcal{V}_{\text{init}} = \{\mathbf{h}_v^{(0)}\} \cup \{\mathbf{h}_{\text{BS}}^{(0)}\}$ 
275 5:   for  $l = 1$  to  $2$  do ▷ 2 Graph convolution layers
276 6:     for  $i \in \mathcal{V}$  do
277 7:        $\mathbf{h}_i^{(l)} = \sigma \left( \mathbf{W}^{(l)} \mathbf{h}_i^{(l-1)} + \sum_{j \in \mathcal{N}(i)} \mathbf{U}^{(l)} \mathbf{h}_j^{(l-1)} \right)$ 
278 8:     end for
279 9:   end for
280 10:   $\mathbf{g} = \text{GlobalMeanPool}(\{\mathbf{h}_i^{(2)}\}_{i=1}^{|\mathcal{V}|})$  ▷ Aggregate graph information
281 11:   $\mathbf{g}_{\text{prompt}} = \text{MLP}_{\text{proj}}(\mathbf{g}; \mathbf{W}_{\text{proj}})$  ▷ Project to prompt dimension
282 12:  return  $\mathbf{g}_{\text{prompt}}$ 
283 13: end procedure

```

---

298 Figure 4: The pipeline of geographic prompt generation.  
299

300 The process begins with the construction of a heterogeneous graph  $\mathcal{G} = (\mathcal{V}, \mathcal{E})$  that encodes the spatial 301 configuration of a given scene. The scene is defined by a 3D building mesh  $\mathcal{M}$ , represented by a 302 set of vertices  $\{\mathbf{v}_i\}_{i=1}^V$  where each  $\mathbf{v}_i \in \mathbb{R}^3$ , and the positions of  $T$  base stations, denoted as  $\mathbf{P}_{\text{BS}} = 303 \{\mathbf{p}^t\}_{t=1}^T$  where each  $\mathbf{p}^t \in \mathbb{R}^3$ . The node set of the graph is the union of these building vertices and 304 base station positions:  $\mathcal{V} = \{\mathbf{v}_1, \dots, \mathbf{v}_V\} \cup \{\mathbf{p}^1, \dots, \mathbf{p}^T\}$ . To capture the inherent proximity 305 relationships in 3D space, the edge set  $\mathcal{E}$  is constructed using Delaunay triangulation over the node set  $\mathcal{V}$ , 306 formally defined as  $\mathcal{E} = \{(i, j) \mid \text{nodes } i \text{ and } j \text{ are connected in the Delaunay triangulation of } \mathcal{V}\}$ . 307

308 The GCN update rule for each layer is formally defined as:

$$309 \mathbf{H}^{(l+1)} = \sigma \left( \tilde{\mathbf{D}}^{-\frac{1}{2}} \tilde{\mathbf{A}} \tilde{\mathbf{D}}^{-\frac{1}{2}} \mathbf{H}^{(l)} \mathbf{W}^{(l)} \right)$$

310 where  $\tilde{\mathbf{A}} = \mathbf{A} + \mathbf{I}$  is the adjacency matrix with self-connections,  $\tilde{\mathbf{D}}$  is the degree matrix of  $\tilde{\mathbf{A}}$ , and 311  $\mathbf{W}^{(l)}$  are the trainable weights of layer  $l$ .

312 The generated geographic prompt  $\mathbf{g}_{\text{prompt}} \in \mathbb{R}^{D_p}$  is integrated into the pre-trained Transformer's 313 input sequence. The complete input sequence  $\mathbf{T}_{\text{input}} \in \mathbb{R}^{(1+1+L) \times D}$  is constructed by prepending 314 the prompt to the existing sequence. It consists of the frozen classification token  $\mathbf{t}_{\text{cls}}$ , the trainable 315 geographic prompt token  $\mathbf{T}_{\text{geo}} = \mathbf{g}_{\text{prompt}}$  (for a single prompt), and the frozen sequence of CSI 316 measurement tokens  $\mathbf{T}_{\text{CSI}}$ . This combined sequence is then added to the frozen positional encoding 317  $\mathbf{E}_{\text{pos}}$ :

$$318 \mathbf{T}_{\text{input}} = [\mathbf{t}_{\text{cls}}; \mathbf{T}_{\text{geo}}; \mathbf{T}_{\text{CSI}}] + \mathbf{E}_{\text{pos}}$$

319 The self-attention mechanism then operates on this extended sequence. The Query ( $\mathbf{Q}$ ), Key ( $\mathbf{K}$ ), 320 and Value ( $\mathbf{V}$ ) matrices are derived by projecting the input sequence with the frozen pre-trained 321 weight matrices  $\mathbf{W}^Q$ ,  $\mathbf{W}^K$ , and  $\mathbf{W}^V$ :

$$322 \mathbf{Q} = \mathbf{T}_{\text{input}} \mathbf{W}^Q, \quad \mathbf{K} = \mathbf{T}_{\text{input}} \mathbf{W}^K, \quad \mathbf{V} = \mathbf{T}_{\text{input}} \mathbf{W}^V$$

324 The attention output is computed as  $\text{Attention}(\mathbf{Q}, \mathbf{K}, \mathbf{V}) = \text{softmax}\left(\frac{\mathbf{Q}\mathbf{K}^T}{\sqrt{d_k}}\right)\mathbf{V}$ .  
 325

326 The parameter efficiency of this approach is a key advantage. The only parameters updated during  
 327 fine-tuning are those of the GNN ( $\theta_{\text{gnn}}$ ), the projection MLP ( $\theta_{\text{proj}}$ ), and the task-specific head ( $\theta_{\text{task}}$ ).  
 328 The optimization process is formulated as:

$$329 \quad \min_{\theta_{\text{gnn}}, \theta_{\text{proj}}, \theta_{\text{task}}} \mathbb{E}_{(\mathbf{X}, \mathcal{M}, \mathbf{P}_{\text{BS}}, \mathbf{y}) \sim \mathcal{D}_{\text{task}}} [\mathcal{L}_{\text{task}}(f(\mathbf{X}, \mathcal{M}, \mathbf{P}_{\text{BS}}), \mathbf{y})]$$

331 where the complete forward pass is defined as  $f(\mathbf{X}, \mathcal{M}, \mathbf{P}_{\text{BS}}) = f_{\theta_{\text{task}}}(f_{\theta_{\text{enc}}}([\mathbf{T}_{\text{geo}}; \mathbf{T}_{\text{CSI}}]))$ .  
 332

### 333 3.5 TASK-SPECIFIC ADAPTATION

335 We design specialized output heads to handle different localization scenarios. For single-base station  
 336 localization, the user equipment position is directly predicted from the final [CLS] token using a  
 337 simple MLP head:

$$339 \quad \hat{\mathbf{p}}_{\text{UE}} = \text{MLP}_{\text{single}}(\mathbf{t}_{\text{cls}}; \mathbf{W}_{\text{single}}) \quad (8)$$

341 For multi-base station scenarios, we employ an attention-based fusion mechanism that dynamically  
 342 integrates information from all available base stations. The process begins by extracting the [CLS]  
 343 tokens from all  $T$  base stations and stacking them into a tensor  $\mathbf{B} \in \mathbb{R}^{T \times D}$ . We then compute  
 344 attention weights  $\alpha_t$  for each base station using a learned attention function:

$$345 \quad \alpha_t = \frac{\exp(\mathbf{v}^T \tanh(\mathbf{W}_{\text{attn}} \mathbf{t}_{\text{cls}}^{(t)}))}{\sum_{j=1}^T \exp(\mathbf{v}^T \tanh(\mathbf{W}_{\text{attn}} \mathbf{t}_{\text{cls}}^{(j)}))} \quad (9)$$

349 Each base station's [CLS] token is processed independently through dedicated MLP heads to gen-  
 350 erate preliminary position estimates  $\hat{\mathbf{p}}_{\text{UE}}^{(t)}$ . The final position estimate is obtained through weighted  
 351 fusion:

$$353 \quad \hat{\mathbf{p}}_{\text{UE}} = \sum_{t=1}^T \alpha_t \cdot \text{MLP}_{\text{multi}}^{(t)}(\mathbf{t}_{\text{cls}}^{(t)}; \mathbf{W}_{\text{multi}}^{(t)}) \quad (10)$$

356 This attention mechanism allows the model to dynamically prioritize contributions from different  
 357 base stations based on their signal quality and geometric configuration, with stations having stronger  
 358 signals or more favorable geometric relationships receiving higher weights. The comprehensive  
 359 framework demonstrates how self-supervised pre-training combined with geographic-aware prompt  
 360 tuning can achieve robust wireless localization across diverse environments while maintaining pa-  
 361 rameter efficiency and practical deployability.

## 363 4 EXPERIMENTS

365 We conduct comprehensive experiments to evaluate our wireless localization foundation model  
 366 across diverse scenarios. The experiments address four key questions: (1) How does our method  
 367 compare to state-of-the-art approaches? (2) What is the impact of geographic information? (3)  
 368 How effective is our cycle-adaptive masking? (4) How well does our method generalize to new  
 369 environments?

### 371 4.1 DATASETS AND EVALUATION METRICS

373 We evaluate our method on the DeepMIMO dataset (Alkhateeb, 2019), using the O1\_3p5 urban  
 374 scenario for both pre-training and fine-tuning. The dataset provides realistic CSI data generated  
 375 through ray-tracing simulations. Detailed configuration parameters are provided in Appendix B.3.

376 Evaluation metrics include Mean Absolute Error (MAE), Root Mean Square Error (RMSE), and Cu-  
 377 mulative Distribution Function at 1 meter (CDF@1m). All results are averaged over 5 independent  
 378 runs.

378 4.2 MAIN RESULTS  
379380 We compare against OMP (compressed sensing), CNN-based, SWiT (Salihu et al., 2024), and  
381 LWLM (Pan et al., 2025).382 Single-BS localization under NLoS represents one of the most challenging scenarios. As shown in  
383 Table 1, SIGMAP with geographic information achieves an MAE of **1.564 m**, RMSE of **5.675 m**,  
384 and CDF@1m of **60.5%**, outperforming the best baseline (LWLM) by 34.4% in MAE and more  
385 than doubling the CDF@1m.386 The key advantage stems from our NLoS-aware attention mechanism that explicitly models multi-  
387 path propagation:  
388

389 
$$\alpha_i = \frac{\exp(\phi(\mathbf{o}_s^{(i)} \cdot \mathbf{W}_{\text{NLoS}}))}{\sum_j \exp(\phi(\mathbf{o}_s^{(j)} \cdot \mathbf{W}_{\text{NLoS}}))}, \quad (11)$$
  
390  
391

392 which allows the model to differentiate between direct and reflected paths, significantly reducing  
393 positioning ambiguity.  
394395  
396 Table 1: Metrics of Single-BS localization.397  
398 

Method	MAE (m)	RMSE (m)	CDF@1m (%)
SIGMAP (w/ map)	<b>1.564</b>	<b>5.675</b>	<b>60.5</b>
SIGMAP (w/o map)	2.275	8.532	31.0
LWLM	2.382	5.822	25.3
SWiT	2.586	8.967	24.3
CNN	2.943	9.423	21.7
OMP	3.287	9.851	15.4

  
403404 Multi-BS collaboration leverages spatial diversity to overcome NLoS limitations. Table 2 shows  
405 that SIGMAP with map achieves **0.673 m** MAE, **1.099 m** RMSE and **84.5%** CDF@1m, improv-  
406 ing the second-best result (SIGMAP w/o map) by 14.7% in MAE and 7.0 percentage-points in  
407 CDF@1m. As further visualized in Figure 5, SIGMAP dominates accuracy, robustness and preci-  
408 sion simultaneously. The CDF curves are shown in B.5  
409410  
411 Table 2: Metrics of Multi-BS (4-BS) collaborative localization.412  
413 

Method	MAE (m)	RMSE (m)	CDF@1m (%)
SIGMAP (w/ map)	<b>0.673</b>	<b>1.099</b>	<b>84.5</b>
SIGMAP (w/o map)	0.789	1.285	77.5
LWLM	0.828	1.178	75.6
SWiT	1.102	1.368	68.1
CNN	1.398	1.731	59.3
OMP	1.685	2.089	50.6

  
418419  
420 4.3 EFFECTIVENESS OF CYCLE-ADAPTIVE MASKING  
421422 Table 3 compares masking strategies. Cycle-adaptive masking (last row) yields the best trade-off:  
423 **0.673 m** MAE and **84.5%** CDF@1m, outperforming fixed grid or strip masking. Dynamic dis-  
424 ruption of periodic CSI patterns forces the model to learn generalizable features instead of shortcut  
425 interpolation.  
426427  
428 Table 3: Effect of cycle-adaptive masking strategy.429  
430 

Method	MAE (m)	RMSE (m)	CDF@1m (%)
Grid-masking only	0.770	1.176	80.3
Strip-masking only	0.753	<b>0.972</b>	75.3
Adaptive masking	<b>0.673</b>	1.099	<b>84.5</b>

  
431

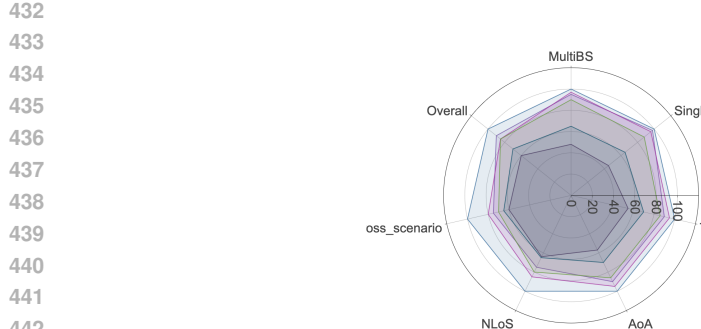


Figure 5: Comprehensive performance comparison across metrics. Our method shows consistent superiority in accuracy and robustness.

#### 4.4 ABLATION STUDY ON MAP PROMPTS

To quantify the influence of map quality on localization accuracy, we conducted an ablative comparison using (i) complete 3-D mesh, (ii) 2-D bird’s-eye polygon, and (iii) no-map (CSI-only). Except for height, the 2-D variant follows the same pipeline as the 3-D version; the gap arises solely from missing height and facade normals.

Two-dimensional and three-dimensional map ablations are illustrated side-by-side in Figure 1. The near-overlapping error bars indicate that most of the topological benefit is retained even without vertical detail. This outcome suggests an immediate upgrade path: replacing the 2-D polygon with a street-level photograph (visual prompt) could re-introduce facade and texture cues, offering a low-cost yet effective extension for future work.

Results are summarised in Table 4: the 2-D bird’s-eye view degrades MAE by 8 % relative to the full 3-D mesh, confirming that most gain comes from topological/LoS cues and that the prompt mechanism is robust to moderate geometric simplification.

Table 4: Single-BS localization with different map modalities.

Method	MAE (m)	RMSE (m)	CDF@1m (%)
SIGMAP (3-D map)	<b>1.564</b>	<b>5.675</b>	<b>60.5</b>
SIGMAP (2-D birdview)	1.692	6.128	55.7
SIGMAP (w/o map)	2.275	8.532	31.0

#### 4.5 GENERALIZATION TO NEW ENVIRONMENTS

We evaluate generalization on two completely unseen ray-tracing suites: (i) DeepMIMO\_O2 scenario and (ii) WAIR-D (Huangfu et al., 2022) Scenario-2 (100 real-world city scenes extracted from OpenStreetMap). Typical complex scenes of WAIR-D are shown in Figure 6, illustrating dense urban canyons and irregular footprints that challenge cross-domain transfer.

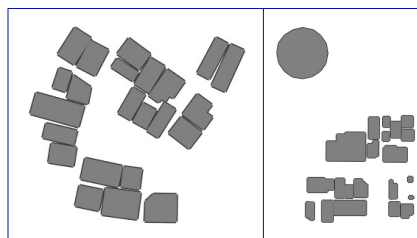


Figure 6: Two typical complex scenes of WAIR-D.

486 In all experiments, only the downstream task heads are fine-tuned using limited target samples (approximately 100 instances per scenario), while the self-supervised backbone remains frozen. This  
 487 few-shot learning setup demonstrates the method’s ability to rapidly adapt to new environments.  
 488 Results are listed in Table 5.  
 489

491 Table 5: Generalization performance on unseen scenarios with minimal fine-tuning.

492 <b>Method</b>	493 <b>MAE (m)</b>	494 <b>RMSE (m)</b>	495 <b>CDF@1m (%)</b>
<i>DeepMIMO O2 outdoor</i>			
SIGMAP (w/ map)	<b>1.026</b>	<b>1.551</b>	<b>66.4</b>
SIGMAP (w/o map)	1.282	5.824	63.9
LWLM	2.213	11.837	63.2
<i>WAIR-D Scenario-2 (100 cities)</i>			
SIGMAP (w/ map)	<b>1.880</b>	<b>3.717</b>	<b>58.0</b>
SIGMAP (w/o map)	2.578	4.650	51.5
LWLM	3.375	6.921	50.3

501 Equipped with geographic prompts, SIGMAP reaches 1.026 m MAE on DeepMIMO O2 and 1.580  
 502 m on WAIR-D Scenario-2, outperforming LWLM by 53.2 % and 44.3 %, respectively, while updat-  
 503 ing only 0.4 % of parameters. The results confirm that, by generating environment-specific prompts,  
 504 SIGMAP delivers good transfer performance across entirely different wireless environments.  
 505

## 506 4.6 PARAMETER EFFICIENCY

509 Table 6: Training cost comparison under our experimental setup.

510 <b>Stage</b>	511 <b>Trainable Params</b>	512 <b>Time/Epoch</b>	513 <b>Total Time</b>
Pre-train	11.730 M	10.8 min	36 h
Fine-tune	0.085 M	1.8 s	30 min
Inference	—	0.83 ms/sample	—

516 Under the experimental setup detailed in Appendix B, the model is first pre-trained for 200 epochs  
 517 and then fine-tuned for 1000 epochs; because only 0.7% of the total parameters are activated during  
 518 fine-tuning, the entire 1000-epoch fine-tuning stage takes merely 30 min, while still preserving the  
 519 rich representations learned during pre-training, demonstrating significant parameter efficiency.  
 520

## 521 5 CONCLUSION

523 This paper presents a wireless localization foundation model that achieves state-of-the-art perfor-  
 524 mance through cycle-adaptive masking and geographic prompt tuning. Our approach delivers strong  
 525 and consistent accuracy in both single-BS and multi-BS tasks, and generalizes robustly across pre-  
 526 viously unseen geographic scenarios.

527 Future work will explore two key directions: extending beyond localization to develop general-  
 528 purpose wireless foundation models for channel estimation, beamforming and signal processing  
 529 tasks; and integrating visual modalities such as images and point clouds with wireless signals to  
 530 create richer environmental representations when 3D maps are incomplete or unavailable.

532 These advances will lead to more versatile and practical wireless perception systems for emerging  
 533 applications in smart infrastructure and mobile computing.

534  
 535  
 536  
 537  
 538  
 539

540 REFERENCES  
541

542 Sadjad Alikhani, Gouranga Charan, and Ahmed Alkhateeb. Large wireless model (LWM): A foun-  
543 dation model for wireless channels. *arXiv preprint arXiv:2411.08872*, 2024.

544 Ahmed Alkhateeb. Deepmimo: A generic deep learning dataset for millimeter wave and massive  
545 mimo applications. *arXiv preprint arXiv:1902.06435*, 2019.

546 Hui Chen, Hadi Sarieddeen, Tarig Ballal, Henk Wymeersch, Mohamed-Slim Alouini, and Tareq Y  
547 Al-Naffouri. A tutorial on terahertz-band localization for 6G communication systems. *IEEE*  
548 *Commun. Surveys Tuts.*, 24(3):1780–1815, 2022a.

549

550 Xi Chen, Hang Li, Chenyi Zhou, Xue Liu, Di Wu, and Gregory Dudek. Fidora: Robust WiFi-  
551 based indoor localization via unsupervised domain adaptation. *IEEE Internet Things J.*, 9(12):  
552 9872–9888, 2022b.

553

554 Yiwen Chen, Tianqi Xiang, Xi Chen, and Xin Zhang. Map-assisted wireless tdoa localization en-  
555 hancement based on cnn. In *2024 IEEE 6th Advanced Information Management, Communicates,*  
556 *Electronic and Automation Control Conference (IMCEC)*, volume 6, pp. 255–260. IEEE, 2024.

557

558 Zirui Chen, Zhaoyang Zhang, Zhuoran Xiao, Zhaojun Yang, and Richeng Jin. Deep learning-based  
559 multi-user positioning in wireless FDMA cellular networks. *IEEE J. Sel. Areas Commun.*, 41(12):  
3848–3862, 2023.

560

561 Jun Gao, Dongze Wu, Feng Yin, Qinglei Kong, Lexi Xu, and Shuguang Cui. MetaLoc: Learning to  
562 learn wireless localization. *IEEE J. Sel. Areas Commun.*, 41(12):3831–3847, 2023.

563

564 Yu Han, Zan Li, Zhongliang Zhao, and Torsten Braun. CrowdBERT: Crowdsourcing indoor posi-  
565 tioning via semi-supervised BERT with masking. *IEEE Internet Things J.*, 11(24):40100–40112,  
2024.

566

567 Lixiong Huang, Ruizhi Chen, Ying Chen, Guangyi Guo, Feng Ye, Zuoya Liu, and Liang Chen. Ro-  
568 bust tdoa-based indoor localization using improved clock-sync-scheme and multilevel constrained  
569 arpf. *IEEE Sensors Journal*, 23(10):10633–10643, 2023.

570

571 Yourui Huangfu, Jian Wang, Shengchen Dai, Rong Li, Jun Wang, Chongwen Huang, and Zhaoyang  
Zhang. Wair-d: Wireless ai research dataset. *arXiv preprint arXiv:2212.02159*, 2022.

572

573 Suhardi Azliy Junoh and Jae-Young Pyun. Enhancing indoor localization with semi-crowdsourced  
574 fingerprinting and GAN-based data augmentation. *IEEE Internet Things J.*, 11(7):11945–11959,  
2024.

575

576 Musa Furkan Keskin, Henk Wymeersch, and Visa Koivunen. MIMO-OFDM joint radar-  
577 communications: Is ICI friend or foe? *IEEE J. Sel. Topics Signal Process.*, 15(6):1393–1408,  
2021.

578

579 Lin Li, Xiansheng Guo, Mengxue Zhao, Huiyong Li, and Nirwan Ansari. Transloc: A heterogeneous  
580 knowledge transfer framework for fingerprint-based indoor localization. *IEEE Trans. Wireless*  
581 *Commun.*, 20(6):3628–3642, 2021.

582

583 Guangjin Pan, Kaixuan Huang, Hui Chen, Shunqing Zhang, Christian Häger, and Henk Wymeersch.  
584 Large wireless localization model (lwlm): A foundation model for positioning in 6g networks.  
585 *arXiv preprint arXiv:2505.10134*, 2025.

586

587 Yanlin Ruan, Liang Chen, Xin Zhou, Zhaoliang Liu, Xiaoyan Liu, Guangyi Guo, and Ruizhi Chen.  
588 iPos-5G: Indoor positioning via commercial 5G NR CSI. *IEEE Internet Things J.*, 10(10):8718–  
8733, 2023.

589

590 Artan Salihu, Markus Rupp, and Stefan Schwarz. Self-supervised and invariant representations for  
591 wireless localization. *IEEE Trans. Wireless Commun.*, 23(8):8281–8296, 2024.

592

593 Jiawei Shao, Jingwen Tong, Qiong Wu, Wei Guo, Zijian Li, Zehong Lin, and Jun Zhang. Wire-  
594 lessllm: Empowering large language models towards wireless intelligence. *arXiv preprint*  
*arXiv:2405.17053*, 2024.

594 Ji Wang, Wei Fang, Jian Xiao, Yi Zheng, Le Zheng, and Fan Liu. Signal-guided masked autoencoder  
 595 for wireless positioning with limited labeled samples. *IEEE Trans. Veh. Technol.*, 74(1):1759–  
 596 1764, 2025.

597 Chi Wu, Xinping Yi, Wenjin Wang, Li You, Qing Huang, Xiqi Gao, and Qing Liu. Learning to  
 598 localize: A 3D CNN approach to user positioning in massive MIMO-OFDM systems. *IEEE*  
 599 *Trans. Wireless Commun.*, 20(7):4556–4570, 2021.

600 Tingting Yang, Ping Zhang, Mengfan Zheng, Yuxuan Shi, Liwen Jing, Jianbo Huang, and Nan Li.  
 601 WirelessGPT: A generative pre-trained multi-task learning framework for wireless communica-  
 602 tion. *arXiv preprint arXiv:2502.06877*, 2025.

603 Xinghang Zhou, Cheng Xu, Jie He, and Jiawang Wan. A cross-region wireless-synchronization-  
 604 based tdoa method for indoor positioning applications. In *2019 28th Wireless and Optical Com-  
 605 munications Conference (WOCC)*, pp. 1–4. IEEE, 2019.

## 608 A STATEMENTS

### 609 A.1 USE OF LLMs STATEMENT

610 We employed large-language-model tools primarily for language polishing and phrasing sugges-  
 611 tions. All technical content, experimental designs, and scientific interpretations were conceived,  
 612 reviewed, and approved by the authors.

### 613 A.2 REPRODUCIBILITY STATEMENT

614 To facilitate reproducibility, we have consolidated the complete pipeline—dataset generation, model  
 615 pre-training, fine-tuning, and evaluation scripts—in an anonymous GitHub repository ([https:////anonymous.4open.science/r/SigMap\\_anonymous-838D](https:////anonymous.4open.science/r/SigMap_anonymous-838D))

## 616 B DETAILED SETUPS OF OUR EXPERIMENTS

### 617 B.1 COMPUTE RESOURCES

618 Our experiments were conducted on a computing server equipped with the following specifications:

- 619 • **GPUs:** 6 × NVIDIA A800 80GB PCIe
- 620 • **GPU Memory:** 80 GB per GPU (480 GB total)
- 621 • **Driver Version:** 550.144.03
- 622 • **CUDA Version:** 12.4

623 The A800 GPUs provided the necessary computational power for training large-scale transformer  
 624 models and processing high-dimensional CSI data with complex shift pattern augmentations.

### 625 B.2 GENERAL CONFIGURATIONS

626 The input to the model is the complex CFR matrix  $\mathbf{H}_s$ . To facilitate neural network processing, we  
 627 decompose it into its magnitude and phase components, denoted as  $\bar{\mathbf{H}}_s$ , and rewrite it as

$$628 \bar{\mathbf{H}}_s = [|\mathbf{H}_s|, \angle \mathbf{H}_s] \in \mathbb{R}^{2 \times N_{\text{ant}} \times N_{\text{subc}}}. \quad (12)$$

629 The input  $\bar{\mathbf{H}}_s$  is a 3D tensor of shape  $(2, N_{\text{ant}}, N_{\text{subc}})$ , with the first dimension corresponding to  
 630 the amplitude and phase, respectively. Although  $\bar{\mathbf{H}}_s$  represents a specific format of the channel  
 631 input, for notational consistency throughout the paper, we will still use  $\mathbf{H}_s$  to refer to the general  
 632 representation of the input channel data in all subsequent discussions.

633 We employed a transformer-based encoder-decoder framework specifically designed for wireless  
 634 channel modeling and localization tasks. The key architectural components include:

648     • **Input Dimensions:**  $B \times C \times T \times F$  where:

649        –  $B$ : Batch size (32)

650        –  $C$ : Channel dimensions (2 for real/imaginary components)

651        –  $T$ : Time/Antenna dimension (128)

652        –  $F$ : Frequency/Subcarrier dimension (32)

653

654     • **Encoder:** Multi-head self-attention layers with positional encoding

655     • **Decoder:** Cross-attention mechanisms for coordinate prediction

656     • **Feature Dimension:** 512-dimensional latent representations

657

658     Table 7: Training Hyperparameters

Parameter	Value
Batch Size	32
Optimizer	Adam
Learning Rate	$1 \times 10^{-4}$
Weight Decay	$1 \times 10^{-5}$
Training Epochs	300
Gradient Clipping	1.0
Learning Rate Schedule	Cosine Annealing
Warm-up Epochs	10

## 669     B.3 DATASET PARAMETERS

670     Table 8: Detailed DeepMIMO dataset configuration parameters

Parameter	Pre-training	Fine-tuning
Scenario	O1_3p5	O1_3p5
Number of BSs	4	4
BS IDs	[3, 4, 9, 10]	[3, 4, 9, 10]
Frequency bands (MHz)	[10, 20, 50]	10
Bandwidth (GHz)	[0.01, 0.02, 0.05]	0.01
Subcarriers	128	128
Antenna elements	32	32
User distribution	Uniform	Random
User subsampling	100%	2%
Number of paths	5	5
CSI samples	480,000	12,000
Train/Val/Test split	-	10,000/1,000/10,00

687     The pre-training data was generated using the following key parameters:

688

689        • Scenario: O1\_3p5 (urban outdoor environment)

690        • Active base stations: 3, 4, 9, 10

691        • Frequency bands: 10MHz, 20MHz, 50MHz

692        • Antenna configuration: 32-element uniform linear array

693        • Subcarrier configuration: 128 subcarriers, all selected

694        • User coverage: Complete row coverage (5200 users)

695

696     Each sample contains complex channel data (real and imaginary components), user and base station  
697     locations, line-of-sight status, distance information, and angle-of-departure parameters.

698     The fine-tuning dataset shares the same environmental scenario but with different sampling strategy:

699

700        • Single frequency band: 10MHz

701

- 702 • User subsampling: 2% of available users
- 703 • Data split: 10,000 training, 1,000 validation, 1,000 test samples
- 704 • Quality filtering: Only samples with valid path information are included

705  
706 The dataset ensures comprehensive coverage of the environment while maintaining realistic user  
707 distribution patterns for effective model evaluation.  
708

#### 709 B.4 DETAILS OF DATA AUGMENTATION EXPERIMENTS

710 CSI amplitude data often exhibits periodicity due to hardware properties of RF chains, such as  
711 antenna spacing and carrier frequency. For instance, in wireless systems with uniform linear arrays,  
712 channel responses between antennas may repeat periodically after a fixed number of antennas.  
713

714 In the process of reconstructing masked channel data using a Vision Transformer (ViT)-based  
715 Masked Autoencoder (MAE), masking only individual rows or columns could allow the model to  
716 easily learn superficial periodic patterns, thereby failing to capture global features from redundant  
717 information.  
718

719 To address this, we adopted a classical time-series method: computing the cross-correlation coeffi-  
720 cient between each row of the Channel Frequency Response (CFR) matrix and the next row. Given  
721 that each row has the same length, significant boundary effects emerge. To mitigate this, we re-  
722 stricted comparisons only to valid regions, avoiding boundary artifacts. In the example provided,  
723 row shifts vary (e.g.,  $d = 8$ ,  $d = -3$ ,  $d = 0$ , see Fig. 7), which can be positive, negative, or zero. This  
724 motivated our adaptive masking strategy.

725 When the bandwidth equals the row-wise shift amount, adjacent masked bands connect end-to-end,  
726 forming visually continuous diagonal strips without gaps. This represents the minimum critical  
727 width required to achieve solid and continuous masking. The shift pattern augmentation technique  
728 is mathematically formulated as follows:  
729

$$730 M_{\text{shift}} = \text{GenerateShiftMask}(d, N_a, N_s, T, F) \quad (13)$$

731 where:

- 732 •  $d$ : Slope parameter controlling shift direction and magnitude
- 733 •  $N_a$ : Number of antenna-based masks (8)
- 734 •  $N_s$ : Number of subcarrier-based masks (32)
- 735 •  $T$ : Time dimension size (128)
- 736 •  $F$ : Frequency dimension size (32)

737 The shift pattern generation algorithm proceeds through these steps:  
738

##### 739 1. Parameter Initialization:

$$740 \text{Bandwidth } bw = |d| \\ 741 \text{Half-bandwidth } hw = \lfloor bw/2 \rfloor \\ 742 \text{Padding } P = hw$$

##### 743 2. Matrix Padding: Expand frequency dimension to accommodate shifts:

$$744 F_{\text{padded}} = F + 2P \quad (14)$$

##### 745 3. Antenna-based Mask Generation: For $i = 1$ to $N_a$ :

$$746 \text{Start column } c_0 \sim \mathcal{U}(0, F) \quad (15)$$

$$747 \text{Column positions } c(t) = c_0 - t \cdot d + P \quad (16)$$

$$748 \text{Mask band } B(t) = [c(t) - hw, c(t) + hw] \cap [0, F_{\text{padded}}] \quad (17)$$

756 4. Subcarrier-based Mask Generation: For  $j = 1$  to  $N_s$ :

757  $\text{Start row } r_0 \sim \mathcal{U}(0, T)$  (18)

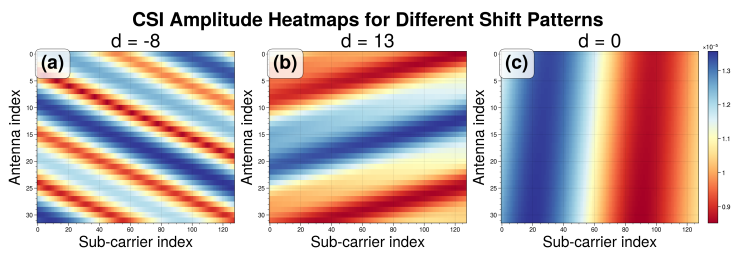
759  $\text{Column positions } c(t) = (t - r_0) \cdot (-d) + P$  (19)

760  $\text{Mask band } B(t) = [c(t) - hw, c(t) + hw] \cap [0, F_{\text{padded}}]$  (20)

761 5. Mask Application: The final augmented input is computed as:

763  $X_{\text{augmented}} = X \odot M + (1 - M) \odot T_{\text{mask}}$  (21)

764 where  $T_{\text{mask}}$  represents learnable mask tokens.

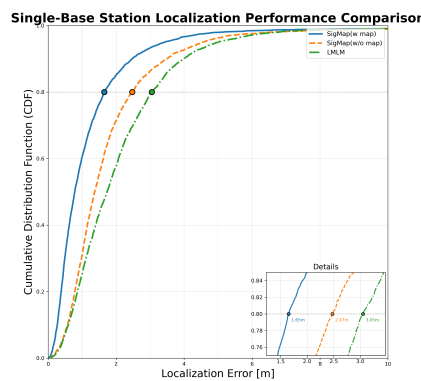


785 Figure 7: CSI Amplitude Heatmaps for Different Shift Patterns

786

### 787 B.5 LOCALIZATION ERROR CDF CURVES

788 The Cumulative Distribution Function (CDF) of localization error measures the probability that the  
 789 positioning error is less than or equal to a given distance. It is the key metric used in Section 4.2  
 790 (Main Results) to compare accuracy and robustness across methods. Figures 8 and 9 plot these CDFs  
 791 for single-BS and 4-BS collaborative scenarios, respectively. A steeper curve and higher value at  
 792 1 m indicate better performance; SIGMAP (w/ map) reaches 60.5% and 84.5% CDF@1m in the two  
 793 settings, clearly outperforming all baselines.



888 Figure 8: Single-Base Station Localization Performance Comparison

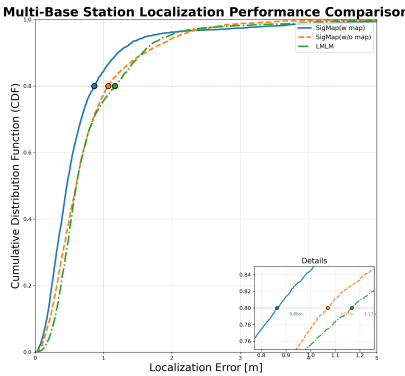


Figure 9: Multi-Base Station Localization Performance Comparison

## C CHARACTERISTICS OF CHANNEL DATA

Wireless Channel State Information (CSI) data exhibits unique characteristics that distinguish it from conventional vision or language modalities and even from generic time series and spatio-temporal data. These traits motivated the antenna–subcarrier joint masking used in SigMap.

### C.1 UNIQUE DIMENSIONALITY: SPATIAL-TEMPORAL-SPECTRAL STRUCTURE

A CSI tensor  $\mathcal{H}$  captured by a multi-antenna OFDM system is inherently multi-dimensional, spanning three critical domains:

- **Spectral Domain (Subcarriers):** Represents the frequency-selective fading of the channel. The correlation across subcarriers  $k$  is a function of the delay spread  $\tau_{\max}$  of the multipath environment, often modeled by the channel’s frequency correlation function.
- **Spatial Domain (Antennas):** Captures the geometric aspects of the propagation. The correlation across antenna elements  $n$  is a function of the angle spread  $\theta_{\text{spread}}$  and array geometry, described by the spatial correlation matrix  $\mathbf{R}_{\text{spatial}} = \mathbb{E}[\mathbf{H}_f \mathbf{H}_f^H]$ .
- **Temporal Domain (Snapshots):** Represents the time-varying nature of the channel due to mobility or environmental changes, characterized by the Doppler spread  $f_d$ .

This structure can be formalized as a 3D tensor  $\mathcal{H} \in \mathbb{C}^{N_{\text{ant}} \times N_{\text{sc}} \times N_{\text{time}}}$ , making it a *Spatial-Temporal-Spectral* data cube. This is distinct from:

- **Time Series:** Which are typically 1D ( $N_{\text{time}}$ ) and lack explicit spatial and spectral structure.
- **Spatio-Temporal Data (e.g., traffic grids, videos):** Which are often 2D+Time ( $Height \times Width \times Time$ ) with spatial homogeneity. The spatial dimensions in CSI are non-grid-like (antenna array geometry) and coupled with the spectral domain.

### C.2 IMPLICATIONS FOR FOUNDATION MODEL DESIGN

The aforementioned characteristics necessitate specialized adaptations in foundation model architecture and pre-training strategies, moving beyond direct applications of models designed for other modalities.

- **Beyond Standard ViT Patches:** While Vision Transformers (ViTs) process images by splitting them into regular 2D patches, this is suboptimal for CSI. Our *cycle-adaptive masking* strategy (Sec. 3.2) is a direct response to this, designed to respect the inherent periodicity and structure within the spatial-spectral planes of the CSI tensor, rather than treating it as a generic image.
- **Beyond Standard MAE for Images:** Masked Autoencoding (MAE) for images relies on the intuition that adjacent pixels are highly correlated. In CSI, the correlation structure

864  
865  
866  
867

is more complex and governed by wireless physics. A random masking strategy fails to exploit the known structure along the antenna and subcarrier dimensions. Our method explicitly leverages this domain knowledge to create a more challenging and meaningful pre-training task.

868  
869  
870  
871  
872  
873

- **Beyond NLP and Time Series Models:** While models for natural language (e.g., GPT) or time series may handle 1D sequences, they are not equipped to natively handle the intertwined 3D correlations present in CSI. The success of SigMap hinges on its ability to simultaneously learn representations across these three domains through its tailored pre-training objectives.

874  
875  
876

In conclusion, the design of SigMap is a principled approach to building a foundation model that respects the unique inductive biases of wireless signal data, rather than forcing the data to conform to architectures designed for fundamentally different modalities.

877  
878  
879  
880  
881  
882  
883  
884  
885  
886  
887  
888  
889  
890  
891  
892  
893  
894  
895  
896  
897  
898  
899  
900  
901  
902  
903  
904  
905  
906  
907  
908  
909  
910  
911  
912  
913  
914  
915  
916  
917